Phase Control of Solid-Solution Nanoparticles beyond the Phase Diagram for Enhanced Catalytic Properties

AUTHOR(S):

Wu, Dongshuang; Kusada, Kohei; Aspera, Susan Meñez; Nakanishi, Hiroshi; Chen, Yanna; Seo, Okkyun; Song, Chulho; ... Kawaguchi, Shogo; Kubota, Yoshiki; Kitagawa, Hiroshi

CITATION:

Wu, Dongshuang ...[et al]. Phase Control of Solid-Solution Nanoparticles beyond the Phase Diagram for Enhanced Catalytic Properties. ACS Materials Au 2022, 2(2): 110-116

ISSUE DATE:

2022-03

URL:

http://hdl.handle.net/2433/276812

ACS MATERIALS Au
AN OPEN ACCESS JOURNAL OF THE AMERICAN CHEMICAL SOCIETY

pubs.acs.org/materialsau Article

Phase Control of Solid-Solution Nanoparticles beyond the Phase Diagram for Enhanced Catalytic Properties

Dongshuang Wu,* Kohei Kusada,* Susan Meñez Aspera, Hiroshi Nakanishi, Yanna Chen, Okkyun Seo, Chulho Song, Jaemyung Kim, Satoshi Hiroi, Osami Sakata, Tomokazu Yamamoto, Syo Matsumura, Yusuke Nanba, Michihisa Koyama, Naoki Ogiwara, Shogo Kawaguchi, Yoshiki Kubota, and Hiroshi Kitagawa*

Cite This: *ACS Mater. Au* 2022, 2, 110–116 Read Online

ACCESS | Metrics & More | Article Recommendations | Supporting Information

ABSTRACT: The crystal structure, which intrinsically affects the properties of solids, is determined by the constituent elements and composition of solids. Therefore, it cannot be easily controlled beyond the phase diagram because of thermodynamic limitations. Here, we demonstrate the first example of controlling the crystal structures of a solid-solution nanoparticle (NP) entirely without changing its composition and size. We synthesized face-centered cubic (fcc) or hexagonal close-packed (hcp) structured Pd_xRu_{1-x} NPs (x = 0.4, 0.5, and 0.6), although they cannot be synthesized as bulk materials. Crystal-structure control greatly improves the catalytic properties; that is, the hcp-Pd_xRu_{1-x} NPs exceed their fcc counterparts toward the oxygen evolution reaction (OER) in corrosive acid. These NPs only require an overpotential (η) of 200 mV at 10 mA cm^{-2}, can maintain the activity for more than 20 h, greatly outperforming the fcc-$Pd_{0.4}Ru_{0.6}$ NPs (η = 280 mV, 9 min), and are among the most efficient OER catalysts reported. Synchrotron X-ray-based spectroscopy, atomic-resolution electron microscopy, and density functional theory (DFT) calculations suggest that the enhanced OER performance of hcp-PdRu originates from the high stability against oxidative dissolution.

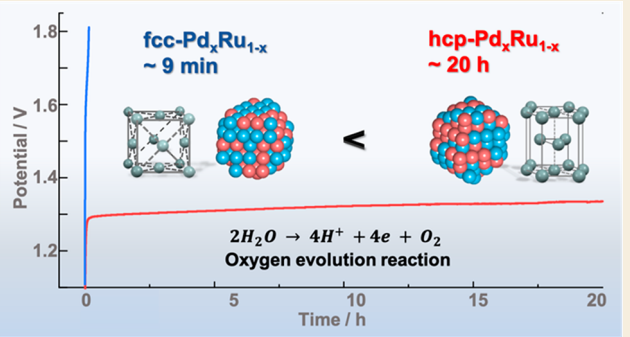

KEYWORDS: *Crystal structure, nanoparticles, alloy, palladium, ruthenium, electrocatalysis, oxygen evolution*

INTRODUCTION

The crystal structure intrinsically correlates to the atomic arrangement and electronic structure of solids.[1] Even in alloy nanoparticles (NPs), the crystal structure is the most important factor among their degrees of freedom, including the size, shape, and composition, and it can significantly boost the emergence of attractive properties for catalysis, electronics, optics, magnetics, and mechanics.[2,3] However, freely tuning the crystal structure is extremely difficult because once the constituent elements and composition of the solids are determined, their crystal structures are thermodynamically fixed. Therefore, to date, controlling the alloy crystal structures beyond the bulk phase diagrams with a fixed composition and size has not been successful in any system. Here, taking Pd (fcc)−Ru (hcp) as a model system, we show the first example of controlling the crystal structure to produce a single fcc or hcp solid-solution structure entirely without changing the composition and size.

Pd and Ru are platinum-group metals that only adopt close-packed structures and never change their bulk structures until their melting points. Given the broad applications of both elements in the fields of magnetic recording, hydrogen storage/separation, biomedicine, and catalysis, there is no doubt that Pd−Ru alloys are some of the most valuable multifunctional binary alloy systems.[4] Their fascinating properties would be further enhanced if the crystal structure of the PdRu alloy could be controlled. However, Pd and Ru are immiscible in the bulk.[5] Recently, Pd_xRu_{1-x} ($0 < x < 1$) metastable solid-solution NPs were obtained, and an individual NP was composed of fcc and hcp domains in a nearly equal ratio in the range $0.3 < x < 0.7$.[6,7] In this study, we report PdRu NPs that comprise a single hcp or fcc structure within this range. As a demonstration, we investigated their oxygen evolution reaction (OER) properties. Pd_xRu_{1-x} alloys exceeded the OER performance of the monometallic Ru and Pd catalysts. Particularly, the hcp-

Received: September 17, 2021
Revised: October 16, 2021
Accepted: October 19, 2021
Published: November 15, 2021

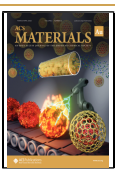

https://doi.org/10.1021/acsmaterialsau.1c00048
ACS Mater. Au 2022, 2, 110–116

$Pd_{0.4}Ru_{0.6}$ NPs require an η of 200 mV at a current density of 10 mA cm^{-2} and can maintain the activity for more than 20 h, greatly outperforming the fcc-$Pd_{0.4}Ru_{0.6}$ NPs (η = 280 mV, 9 min). The performance of hcp-$Pd_{0.4}Ru_{0.6}$ NPs was among the most active OER catalysts reported. The crystal structures and their relationship with the catalytic performance were fully determined and discussed via synchrotron X-ray-based spectroscopy methods, atomic-resolution electron microscopy, and DFT calculations.

RESULTS AND DISCUSSION

Synthesis and General Characterization

Figure 1a shows the process of controlling the crystal structure of Pd_xRu_{1-x} NPs in the metastable mixed-phase area ($0.3 < x <$

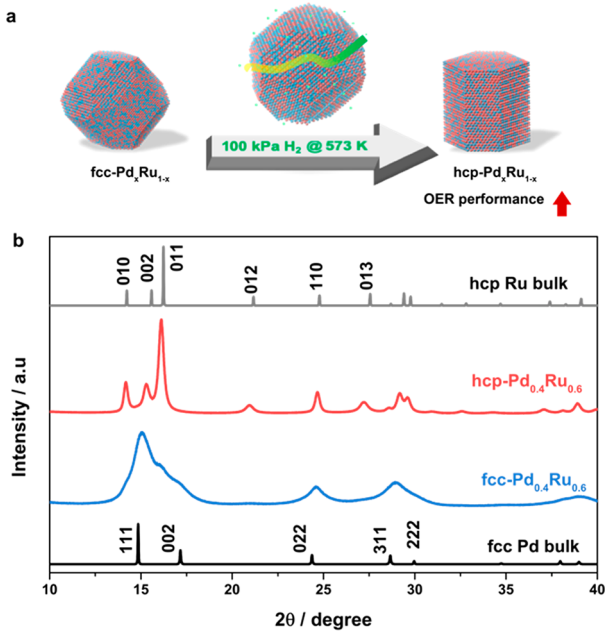

Figure 1. (a) Illustration of the process controlling the crystal structure of Pd_xRu_{1-x} ($0.3 < x < 0.7$) solid-solution NPs for OER. The synthesized fcc-Pd_xRu_{1-x} changed to hcp-Pd_xRu_{1-x} NPs by hydrogen treatment. (b) PXRD patterns in the region of 2θ = 10°–40°. The radiation wavelength was 0.5806(8) Å.

0.7). We first synthesized Pd_xRu_{1-x} (x = 0.4, 0.5 and 0.6, Figures S1 and S2; Table S1) solid-solution NPs by a modified polyol method.[7] The atomic ratios of Pd and Ru in the NPs were determined using an X-ray fluorescence (XRF) spectrometer and are consistent with nominal ratios between metal precursors. The obtained NPs possessed a fcc-dominated structure (denoted as fcc-Pd_xRu_{1-x}, analyses in Figure 3) due to the relatively faster reduction speed of K_2PdCl_4 than $RuCl_3$.[8] Next, hcp structure (denoted as hcp-Pd_xRu_{1-x}) was obtained by heating the fcc-Pd_xRu_{1-x} NPs under H_2 at 573 K. This might be because hcp is a more thermodynamically favorable phase. The Pd–Ru alloy can absorb hydrogen[7] which could accelerate the atomic rearrangement at a low temperature. In contrast, the crystal structure is not changed in vacuum at the same temperature. The synchrotron X-ray diffraction (XRD) patterns showed that the synthesized and hydrogen-treated $Pd_{0.4}Ru_{0.6}$ NPs displayed fcc and hcp patterns, respectively (Figure 1b). Transmission electron microscopy (TEM) images revealed the same particle size for the hcp and fcc NPs (Figure 2), showing that phase transformation was not caused by particle aggregation or growth.

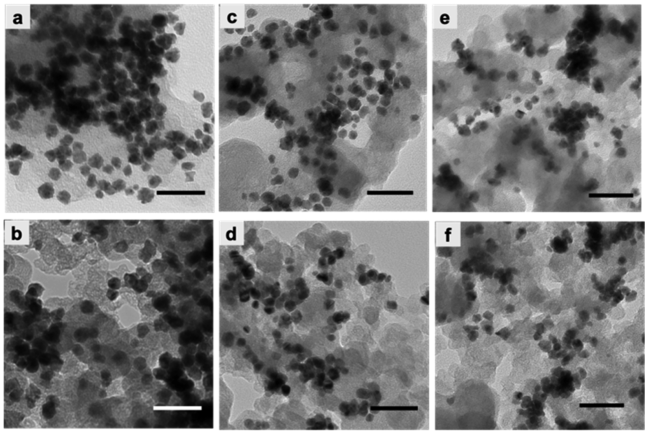

Figure 2. TEM images of carbon-loaded (a) fcc-$Pd_{0.4}Ru_{0.6}$, (b) hcp-$Pd_{0.4}Ru_{0.6}$, (c) fcc-$Pd_{0.5}Ru_{0.5}$, (d) hcp-$Pd_{0.5}Ru_{0.5}$, (e) fcc-$Pd_{0.6}Ru_{0.4}$, and (f) hcp-$Pd_{0.6}Ru_{0.4}$ NPs. The size of fcc-Pd_xRu_{1-x} was not changed after hydrogen treatment. In order to proceed with the catalysis, the as-prepared fcc-Pd_xRu_{1-x} was loaded on carbon. Scale bar: 50 nm.

Bulk and Local Crystal Structure

Rietveld refinement of the XRD pattern of fcc-$Pd_{0.4}Ru_{0.6}$ indicated that 81.9% of the fcc component was present (Figure S4). The lattice parameters for both the fcc and hcp components suggested a Pd:Ru ratio of 0.4:0.6 according to Vegard's law, which agrees with the ratio obtained by XRF (Table S2). The atomic-resolution scanning TEM (STEM) image (Figure 3a) of an individual fcc-$Pd_{0.4}Ru_{0.6}$ NP and the

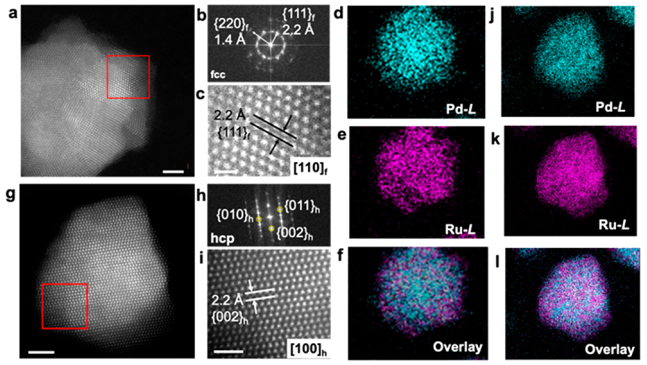

Figure 3. (a) Atomic-resolution STEM image and (b) FFT pattern of an individual NP showing the fcc structure. The planar distances calculated from the radii of the two concentric cycles are 2.2 and 1.4 Å, corresponding to the lattice distances of the $\{111\}_f$ and $\{220\}_f$ planes, respectively. (c) Magnified image of the red squared area in (a). (g)–(i) Atomic-resolution STEM image, FFT pattern, and magnified image of an individual NP showing a hcp structure. EDX maps of an individual (d–f) fcc-$Pd_{0.4}Ru_{0.6}$ and (j–l) hcp-$Pd_{0.4}Ru_{0.6}$ NP showing Pd-*L* (green), Ru-*L* (red), and overlay images. The scale bar is 2 nm in (a) and (g), 0.5 nm in (c), and 1 nm in (i).

corresponding concentric-circle type fast Fourier transform (FFT) pattern (Figure 3b) showed a polycrystalline fcc nature. The calculated *d*-spacings from the two circles in the FFT pattern are estimated to be the $\{111\}_f$ (f stands for fcc) (2.2 Å) and $\{200\}_f$ (1.4 Å) planes. A magnified STEM image further shows a typical fcc atomic arrangement from the $[110]_f$ zone

https://doi.org/10.1021/acsmaterialsau.1c00048
ACS Mater. Au 2022, 2, 110–116

axis (Figure 3c). A twin boundary ($(111)_f$ facet) in the polycrystalline fcc structure is identical to the $(001)_h$ facet of the hcp structure. Therefore, the fcc component percentage should be underestimated by XRD refinement and pure hcp or hcp-dominated NPs were not observable by STEM. Energy dispersive X-ray (EDX) maps showed the random distribution of Pd and Ru atoms (Figure 3d–f), which also confirmed the solid-solution nature.

The XRD pattern of the H_2-treated sample was refined by a single hcp component with a Pd: Ru ratio of 0.4:0.6 (Figure S4), which suggests the solid-solution nature. The STEM image of an individual hcp-$Pd_{0.4}Ru_{0.6}$ NP (Figure 3g) exhibits a FFT pattern corresponding to the $[100]_h$ (h stands for hcp) crystal zone (Figure 3h). The closed-packed planes stacked with the ABAB... sequence with an interplanar spacing of 2.2 Å correspond to the $\{002\}_h$ planes, which is consistent with the XRD refinement results (Figure 3i and Table S3). EDX maps also confirmed solid solution formation (Figure 3j–l). It is worth noting that hcp-$Pd_{0.4}Ru_{0.6}$ is not a hydride because it has a similar atomic distance to that of the fcc-$Pd_{0.4}Ru_{0.6}$ NPs. These results showed the successful crystal structure control of PdRu solid-solution alloys at a fixed composition and size within individual NPs.

Electronic Structures

Hard X-ray photoelectron spectroscopy (HAXPES) measurements were conducted to investigate the intrinsic electronic structure. The Pd3d and Ru3p core-level spectra of the fcc- and hcp-$Pd_{0.4}Ru_{0.6}$ NPs overlapped, and both spectra showed metallic features of Pd and Ru elements (Figure S5).[9] The valence band (VB) features of the $Pd_{0.4}Ru_{0.6}$ NPs are distinguished from those of monometallic NPs as well as the summation of Pd and Ru spectra standing for a physical mixture (black line) (Figure 4a). This suggests the hybridization of the Pd and Ru orbitals because of the formation of a solid solution. The similarity in the electronic structure reflecting from both core-level spectra and VB spectra is because both fcc and hcp are close-packed structures.[10] Still, there are some differences between fcc-and hcp-$Pd_{0.4}Ru_{0.6}$ NPs in the VB spectra. hcp-$Pd_{0.4}Ru_{0.6}$ NPs had a deeper *d*-band center than that of fcc-$Pd_{0.4}Ru_{0.6}$ (−4.16 vs −4.04 eV). We further focused on the region near the Fermi level (E_F) (0–2 eV). hcp-$Pd_{0.4}Ru_{0.6}$ had a lower density of states (DOS) than that of fcc-$Pd_{0.4}Ru_{0.6}$ (Figure 4a, yellow region in dotted box).

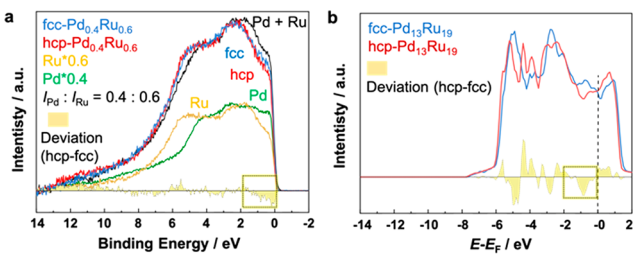

Figure 4. (a) Experimental HAXPES VB spectra. The black line is a summation of Pd (green) and Ru (yellow) HAXPES VB spectra, which stands for a physical mixture of Pd and Ru in the atomic ratio of 4:6. (b) Theoretical HAXPES VB spectra using a random alloy configuration of Pd and Ru. Here, the yellow areas in (a) and (b) indicate the difference in VB spectra between the hcp- and fcc-$Pd_{0.4}Ru_{0.6}$ NPs. The dotted boxes outline the range of 0–2 eV near the Fermi level.

The DFT-based calculation of DOS was carried out to gain a deeper understanding of the electronic states of PdRu NPs. We adopted $Pd_{13}Ru_{19}$ in fcc and hcp models using random alloy configurations. The DOS in Figure 4b shows the two main features of PdRu at −2.5 and −5 eV, which is consistent with the observed spectra in Figure 4a. Without the limitation of experimental spectral resolution, the calculated spectrum of hcp-$Pd_{13}Ru_{19}$ shows a clearer difference from that of fcc-$Pd_{13}Ru_{19}$. Therefore, the intrinsic differences in the electronic structure between fcc- and hcp-PdRu were confirmed using both experimental VB spectra and calculated DOS. This result implies that the Pd and Ru orbital hybridization changed when the atomic rearrangement alters from ABCABC to ABAB stacking.

OER Activity and Stability

Ru is one of the most active metals for OER but cannot be practically used because of severe degradation problems, especially in acids.[11] Stabilizing OER catalysts in acids is a major task in the electrochemistry field. Here, we show that the hcp-Pd_xRu_{1-x} NPs exhibited a markedly enhanced performance, especially regarding durability, toward the OER in the corrosive acid, which greatly exceeded that of not only their fcc counterparts but also most Ru metal catalysts.

The OER activity was recorded by the quasi-stationary scan of linear sweep voltammetry (LSV) in O_2-saturated 0.1 M $HClO_4$.[12] The Cu underpotential (UPD) experiments showed that fcc- and hcp-$Pd_{0.4}Ru_{0.6}$ NPs had almost the same electrochemical active surface area (EASA) (Figure S6). Thus, the OER current is normalized by the geometric area of electrodes (0.196 cm^2). When the LSV was conducted from low to high potential, Ru NPs showed a peak at around 1.45 V in the first LSV curve and quickly lost the activity thereafter because of the severe oxidation and elution of Ru NPs (Figure S7).[11] Therefore, we performed the cathodic LSV scans (from high to low potential) to minimize the contribution of metal oxidation current to the observed current. The hcp-$Pd_{0.4}Ru_{0.6}$ reached 10 mA cm^{-2}_{geo} at η of 200 mV and showed higher activities than fcc-$Pd_{0.4}Ru_{0.6}$ (η = 280 mV), Ru NPs (η = 538 mV), and Pd NPs (η = 530 mV) (Figure 5a). The large overpotential of Pd NPs reflects the low activity, although Pd has better stability than Ru. Both hcp- and fcc-$Pd_{0.4}Ru_{0.6}$ NPs showed higher activity than monometallic NPs, suggesting advantages of the alloys. The high activity of hcp-$Pd_{0.4}Ru_{0.6}$ outperforms the reported highly active catalysts, for example, $IrNiO_x$ (>330 mV),[12] $Y_2Ru_2O_{7-\delta}$ (>370 mV),[13] IrO_x/$SrIrO_x$ (270–290 mV),[14] and laminar Ir NPs (270 mV).[15]

To further understand the high activity of hcp-$Pd_{0.4}Ru_{0.6}$ NPs, we conducted rotating ring disk electrode experiments. When the disk was positively scanned to a high potential, the oxidation of H_2O_2, that is, current density collected from the ring electrode (at a fixed ring potential of 1.48 V), is less than 0.1 mA cm^{-2} (Figure S8a). The yield of H_2O_2 was below 1% after 1.50 V. The electron transfer number is 4 (Figure S8b). These results suggested the exclusive product as O_2. The faradaic efficiency (FE) of OER catalyzed by hcp-$Pd_{0.4}Ru_{0.6}$ NPs was calculated to be as high as 98.9% based on the ratio of ring and disk current (at a fixed ring potential of 0.4 V, Figure 5b,c), which shows that the observed current mainly comes from OER rather than metal oxidation.

The durability was evaluated by chronopotentiometry measurements. The hcp-$Pd_{0.4}Ru_{0.6}$ NPs retained a current density of 1 mA cm^{-2} for more than 20 h and 10 mA cm^{-2} for

https://doi.org/10.1021/acsmaterialsau.1c00048
ACS Mater. Au 2022, 2, 110–116

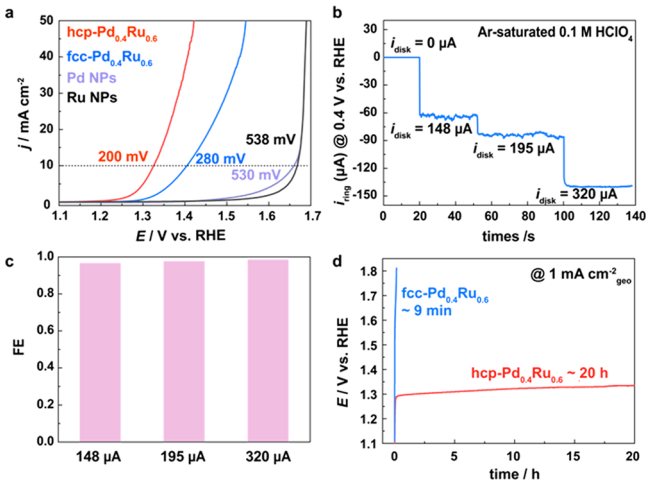

Figure 5. (a) Polarization curves of the as-prepared fcc-$Pd_{0.4}Ru_{0.6}$, hcp-$Pd_{0.4}Ru_{0.6}$, Ru, and Pd NPs. Measurement conditions: 1600 rpm, 5 mV/s, O_2-saturated 0.1 M $HClO_4$, negative scan. (b) Ring current of hcp-$Pd_{0.4}Ru_{0.6}$ with varying disk currents in Ar-saturated 0.1 M $HClO_4$ (ring potential: 0.4 V vs RHE). (c) Calculated FE from the data in (b). The FE at 148, 195, and 320 μA was 97.0%, 97.3%, and 98.9%, respectively. (d) CP measurement at a fixed current density of 1 mA cm^{-2}.

6 h (with less than 5% potential increase) (Figures 5d and S9). This durability is comparable to the reported efficient Ru- or Ir-based catalysts, such as $IrNiO_x$ (20 h @1 mA cm^{-2}),[12] IrO_x/ATO (15 h @1 mA cm^{-2}),[16] $Y_2Ru_2O_{7-\delta}$ (8 h @1 mA cm^{-2}_{oxide}),[13] Cu-doped RuO_2 (8 h @10 mA cm^{-2}),[17] and Ir nanowires (5.6 h @10 mA cm^{-2}).[18] In contrast, the electrode potential of fcc-$Pd_{0.4}Ru_{0.6}$ NPs quickly increased to 1.8 V within 9 min, suggesting serious catalytic deterioration. This result showed that hcp-$Pd_{0.4}Ru_{0.6}$ had enhanced durability compared to fcc-$Pd_{0.4}Ru_{0.6}$. Similarly, both hcp-$Pd_{0.6}Ru_{0.4}$ and hcp-$Pd_{0.5}Ru_{0.5}$ showed higher catalytic durability and/or activity than their corresponding fcc counterparts (Figures S10–S17).

Experimental and Theoretical Analyses for OER Performance

O_2 generation accompanies the oxidation of metal catalysts. However, Ru is easily oxidized to high-valence oxides at a low potential, such as water dissolvable RuO_4 (the thermal equilibrium potential is 1.4 V in pH = 1 electrolyte), and thus, severe catalysts dissolution occurs.[19−21] Basically, the dissolution directly relates to the durability of a catalyst. However, for most Ru-based nanocatalysts, the catalyst loading amount on the electrodes sharply decreases because of the dissolution, which leads to the decreased geometric activity. Therefore, the oxidation states and rate directly relate to the OER activity and durability of the Ru-based catalysts. To both qualitatively and quantitatively understand the oxidation states, we adopted X-ray absorption near-edge spectra (XANES) after the accelerated durability test (ADT, Figure S18) of OER.[12,22] The absorption edge (defined as the first infection point in the spectrum) of the Ru K-edge for hcp-$Pd_{0.4}Ru_{0.6}$ after ADT is 1.34 eV more negative than that of hcp-$Pd_{0.4}Ru_{0.6}$ (Figure 6a). Moreover, in the XANES spectrum of hcp-$Pd_{0.4}Ru_{0.6}$, the energy separation and amplitude oscillation between the first two peaks (ca. 22 133 and 22 157 eV) are wider and deeper compared to those for the fcc-$Pd_{0.4}Ru_{0.6}$; that is, the XANES spectrum features were closer to those for Ru metal. These

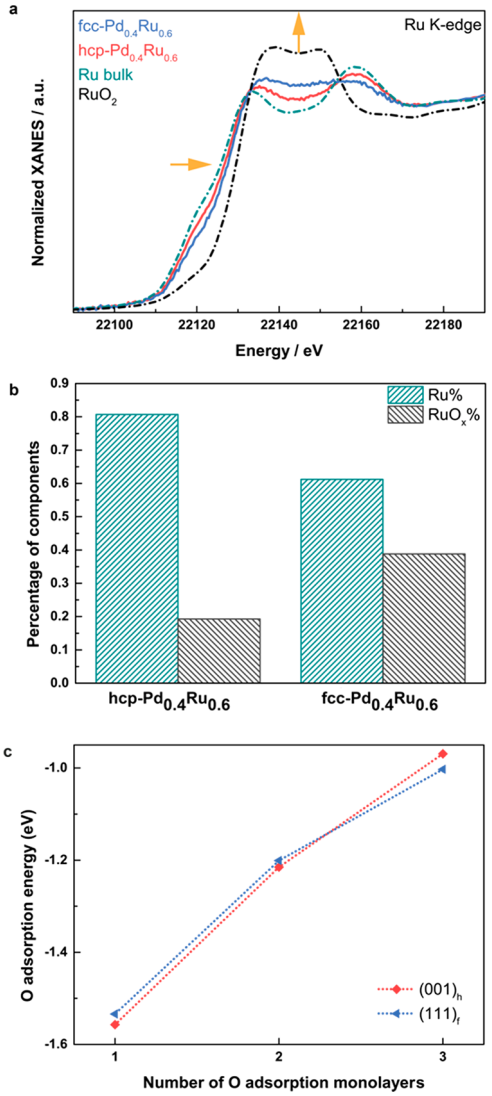

Figure 6. (a) Ru K-edge XANES spectra of fcc- and hcp-$Pd_{0.4}Ru_{0.6}$ after OER. (b) Percentage of Ru and RuO_2 components in fcc- and hcp-$Pd_{0.4}Ru_{0.6}$ obtained by LCF. (c) O adsorption energy on different facets with an increasing number of O content, i.e., from 1 to 3 monolayers.

results indicated that hcp-$Pd_{0.4}Ru_{0.6}$ had a lower valence state after ADT than fcc-$Pd_{0.4}Ru_{0.6}$. Linear combination fitting of XANES further qualitatively showed that hcp-$Pd_{0.4}Ru_{0.6}$ consisted of 19% metal oxides and 81% metal, while fcc-$Pd_{0.4}Ru_{0.6}$ had only 61% metal (Figures 6b and S19). XANES analyses suggested that Ru is less oxidized in hcp-$Pd_{0.4}Ru_{0.6}$ than in fcc-$Pd_{0.4}Ru_{0.6}$ NPs. To support our discussion on the oxidation rate, we measured atomic-resolution STEM images of the PdRu catalysts after ADT. The size distribution of hcp-$Pd_{0.4}Ru_{0.6}$ NPs is 12.8 ± 2.4 nm (Figure S20a) after ADT. The STEM image showed that the hcp-$Pd_{0.4}Ru_{0.6}$ NPs was composed by an amorphous thin outer layer and crystalline core (Figure S21a, b). Based on the results of XANES, this amorphous layer can be attributed to the oxidized layer. For fcc-$Pd_{0.4}Ru_{0.6}$, fewer NPs with greatly decreased particle size (4.2 ± 1.4 nm, Figure S20b) were observed on carbon and most particles had a thicker amorphous oxides layer (Figure S21c,d). . We note that the percentage of RuO_x is not directly related to the activity, although RuO_x is considered as an active

https://doi.org/10.1021/acsmaterialsau.1c00048
ACS Mater. Au 2022, 2, 110−116

species for OER. The STEM and TEM observations are consistent with the XANES results, which indicates that the hcp-$Pd_{0.4}Ru_{0.6}$ is more resistant to forming the easily dissolvable high-valence metal oxides.

The fcc- and hcp-PdRu NPs show distinct OER performance, even though they have almost the same size, composition, core-level electronic states, and EASA. Although fcc-PdRu has a smaller crystal size and more crystal domains than hcp-PdRu NPs, a similar EASA suggests that the interfaces between crystal domains do not contribute to the surface area. In other words, crystal size might not largely influence the activity of fcc- and hcp-PdRu. NPs are reported to have worse OER durability than their bulk counterpart,[11] which leads to the conclusion on the importance of crystal size. However, the crystal size might not be the main contributor for stability especially when the crystal size is below 10 nm in Ru-based NPs.[22] Therefore, theoretical calculations were employed to provide in-depth insights into the effect of the crystal structure on the stability of the PdRu alloy against oxidation during OER. It is generally acknowledged that most Ru-based OER catalysts start to dissolve after the formation of stable metal oxides, such as RuO_2.[20,23] Based on both experimental data using single-crystalline Ru surfaces and theoretical calculations,[24,25] previous studies suggest that the mechanism of oxidation of a highly packed surface such as the $(001)_h$ surface to RuO_2 rutile (110) involves a series of metastable precursor states and follows three steps starting from the surface metal layer, i.e., 3 monolayers (MLs) of oxygen adsorption (see details in the Supporting Information). Therefore, as an important intermediate step toward the formation of a stable metal oxide structure, we compared the oxygen adsorption energy for an increasing number of O concentrations via the formation of 1−3 MLs[26] on both PdRu $(111)_f$ and $(001)_h$ surfaces,[27] which are close-packed facets with the lowest surface energies in the fcc and hcp structure, respectively (Figures S22 and S23). The 2 ML O adsorption represents the formation of RuO_2, and it was destabilized by adding 3 ML O. Upon increasing the O content from 1 to 3 ML, we could observe a shift in the trend of O stability. As shown in Figure 6c, hcp-PdRu$(001)_h$ has a relatively higher energy to form 3 ML compared with fcc-PdRu$(001)_f$. This trend is expected to occur even for higher O content, which suggests that hcp-PdRu has higher stability against oxidative dissolution than fcc-PdRu. This theoretical study supports the experimental results.

CONCLUSION

In summary, we reported controlling the crystal structure in a nonequilibrium solid-solution system over the entire mixed-phase region. The fcc-Pd_xRu_{1-x} solid-solution NPs transformed to hcp structures by hydrogen treatment. The transformation took place within individual NPs without any NP size change, which enabled us to study the catalytic properties free from the size effect. hcp-Pd_xRu_{1-x} is a highly active and stable OER catalyst delivering 10 mA cm^{-2}_{geo} with only 200 mV overpotential, which exceeds its fcc counterpart and is among the most active OER catalysts. Such an enhancement is mainly attributed to the crystal structure related surface structure and electronic structure revealed by HAXPES, XANES, and DFT calculations. Beyond the scope of binary alloys, our study could have far-reaching implications for multiple-element alloys used for a wide variety of applications.

EXPERIMENTAL METHODS

Synthesis of fcc-Pd_xRu_{1-x}, Pd, and Ru NPs

In a typical synthesis of fcc-$Pd_{0.4}Ru_{0.6}$ NPs, K_2PdCl_4 (1.0 mmol, 326 mg) and $RuCl_3 \cdot nH_2O$ (1.2 mmol, 392 mg, Wako) were dissolved in deionized water (50 mL). Then, the precursor mixture was added via a syringe pump into a preheated triethylene glycol (TEG, 300 mL, TCI) solution in the presence of poly(*N*-vinyl-2-pyrrolidone) (PVP, 1.11 g, $MW \approx 40\,000$, Wako) at 473 K in air under magnetic stirring.

Pd_xRu_{1-x} (x = 0.4 and 0.5) NPs. Ru NPs were obtained following the same process as $Pd_{0.4}Ru_{0.6}$ NPs except K_2PdCl_4 was not added. Pd NPs were obtained by refluxing K_2PdCl_4 (2.0 mmol, 652 mg) in ethylene glycol (EG, 120 mL, TCI) solution with PVP (2.22 g) for 1 h.

Synthesis of hcp-Pd_xRu_{1-x} NPs

To obtain hcp-$Pd_{0.4}Ru_{0.6}$ NPs, we first loaded the as-prepared Pd_xRu_{1-x} NPs on carbon (Vulcan XC-72R, Cabot) by sonicating the NPs and carbon powder in a mixture of deionized water and 2-propanol (volume ratio of 1:4) for 4 h. After collecting the carbon-loaded Pd_xRu_{1-x} powder by centrifuging and drying, the powder was sealed in 100 KPa hydrogen and heated at 573 K by using a pressure−composition−temperature apparatus (Suzuki Shokan Co., Ltd.). After thermal treatment, we recorded the XRD pattern at room temperature in a vacuum atmosphere to exclude the influence of H_2 absorption by metal NPs. The carbon-supported fcc-$Pd_{0.4}Ru_{0.6}$ NPs were obtained following the same process as for the hcp-$Pd_{0.4}Ru_{0.6}$ NPs, except for changing the heating atmosphere into the vacuum. The carbon-supported $Pd_{0.5}Ru_{0.5}$ and $Pd_{0.6}Ru_{0.4}$ were treated at 673 and 723 K, respectively.

General Characterization

The TEM images were captured by using a Hitachi HT7700 instrument operated at 100 kV. The HRTEM images, atomic resolution STEM images, and EDX maps were taken using a JEM-ARM 200F STEM instrument operated at 200 kV. The atomic ratios of Pd and Ru in the NPs were determined using an XRF spectrometer (ZSX Primus IV, Rigaku). Lab XRD data were collected using *D*8 (Bruker, Germany) with a step size of 0.05° (radiation wavelength, 1.54 Å). Lab XPS spectra were recorded on a Shimadzu ESCA-3400 X-ray photoelectron spectrometer using a monochromatic Mg Kα source of 12543.6 eV at 200 W.

Synchrotron X-ray-Based Spectroscopy Methods

All these experiments were performed at JASRI/SPring-8, Japan. The synchrotron XRD patterns were measured with a radiation wavelength of 0.58 Å at the BL02B2 beamline.[28] The samples were sealed into a ϕ 0.4 mm borosilicate glass capillary tube and tested in a two-step mode with a step size of 0.006° at room temperature. The HAXPES experiments were performed at the National Institute for Materials Science (NIMS) contract undulator beamline BL15XU. The XANES measurements of the Ru K-edge were performed using a Si(311) monochromator crystal at beamline BL14B2. See details of data analyses in the Supporting Information.

Calculated VB Spectra and Computations for the Formation of the Oxides

See details in the Supporting Information.

OER Performance

The catalyst inks were prepared by sonicating the mixture of the catalyst powder (ca. 5.5 mg), deionized water (0.3 mL), 2-propanol (0.6 mL), and Nafion solution (0.1 mL, 5 wt % in lower aliphatic alcohols and H_2O, Sigma-Aldrich) for 30 min. The concentration of metal in the ink was 1 mg/mL. Ten microliters of the catalyst ink was pipetted onto the precleaned glassy carbon surface and dried in air to form a homogeneous thin film. All electrochemical measures were recorded by using a CHI 760e electrochemical workstation (CHI instruments, Inc., USA) connected to an RRDE-3A constant rotation system (ALS Co., Ltd., Japan). We used a traditional three-electrode system, e.g., Ag/AgCl (3 M NaCl), a Pt coiled wire (57 mm in

https://doi.org/10.1021/acsmaterialsau.1c00048
ACS Mater. Au 2022, 2, 110−116

length), and a RDE (5 mm in disk diameter) as the reference, counter, and working electrodes, respectively. The reference electrode was calibrated at room temperature before each trial. Perchloric acid (0.1 M) was used as the electrolyte. The potential in this research was converted to reverse hydrogen electrode (RHE) by using the equation below:

$$E_{RHE} = E_{applied} + 0.195 + 0.0592 \times pH$$

where $E_{applied}$ is the applied potential vs Ag/AgCl, 0.195 V is the standard potential of the Ag/AgCl electrode (3 M NaCl) at 25 °C, and pH is the measured value of 0.1 M $HClO_4$.

Prior to the OER test, each electrode was swept from 0.05 to 1.05 V at a speed of 200 mV/s for several hundred cycles in an Ar-saturated 0.1 M $HClO_4$ solution to obtain a stable and clean electrode surface. To determine the OER performance, all catalysts were subjected to 1.15 V for 3 min, followed by a quasi-stationary linear sweep voltammetry (LSV) scan from high potential to low potential at 5 mV/s and 1600 rpm in an O_2-saturated 0.1 M $HClO_4$. The OER stability was evaluated by the chronopotentiometry (CP) method with a fixed current density of 1 or 10 mA cm^{-2}. For RRDE measurements, the disk electrode (4 mm in disk diameter) was scanned at a rate of 5 mV/s. For the FE evaluation,[29] we monitor the ring current under a constant disk current while the potential of ring was kept at 0.4 V. The FE can be calculated as shown below:

$$FE\ (\%) = 100 \times I_r/(I_d \times N)$$

where I_r and I_d are the ring and disk current, respectively, and N is the transfer electron numbers. The background current density (below 1.2 V), which comes from the capacitance current and oxidation of the metal and carbon before OER, was deducted from the measured LSV, and thus, the current is almost zero before the onset of OER. All the polarization curves were corrected for the *iR* contribution. All the electrochemical measurements were repeated at least three times to confirm the reproducibility.

■ ASSOCIATED CONTENT

Supporting Information

The Supporting Information is available free of charge at https://pubs.acs.org/doi/10.1021/acsmaterialsau.1c00048.

HAXPES and XANES experimental details, theoretical calculation details, TEM, XRD, XPS of as-prepared samples, Cu UPD data, electrochemical data of $Pd_{0.5}Ru_{0.5}$ and $Pd_{0.6}Ru_{0.4}$ NPs, ADT of OER, STEM, and TEM of $Pd_{0.4}Ru_{0.6}$ after catalysts, models of theoretical calculations, and further discussion (PDF)

■ AUTHOR INFORMATION

Corresponding Authors

Dongshuang Wu − *Division of Chemistry, Graduate School of Science, Kyoto University, Kyoto 606-8502, Japan;* orcid.org/0000-0001-8512-8473; Email: dongshuangwu@kuchem.kyoto-u.ac.jp

Kohei Kusada − *Division of Chemistry, Graduate School of Science, Kyoto University, Kyoto 606-8502, Japan;* Present Address: The Hakubi Center for Advanced Research, Kyoto University, Kitashirakawa-Oiwakecho, Sakyo-ku, Kyoto 606−8502, Japan; orcid.org/0000-0002-9679-6749; Email: kusada@kuchem.kyoto-u.ac.jp

Hiroshi Kitagawa − *Division of Chemistry, Graduate School of Science, Kyoto University, Kyoto 606-8502, Japan;* orcid.org/0000-0001-6955-3015; Email: kitagawa@kuchem.kyoto-u.ac.jp

Authors

Susan Meñez Aspera − *National Institute of Technology, Akashi College, Akashi, Hyogo 674-8501, Japan*

Hiroshi Nakanishi − *National Institute of Technology, Akashi College, Akashi, Hyogo 674-8501, Japan;* orcid.org/0000-0001-9843-1527

Yanna Chen − *Synchrotron X-ray Group and Synchrotron X-ray Station at SPring-8, National Institute for Materials Science, Sayo, Hyogo 679-5148, Japan;* orcid.org/0000-0001-7937-4395

Okkyun Seo − *Synchrotron X-ray Group and Synchrotron X-ray Station at SPring-8, National Institute for Materials Science, Sayo, Hyogo 679-5148, Japan;* orcid.org/0000-0002-8732-0255

Chulho Song − *Synchrotron X-ray Group and Synchrotron X-ray Station at SPring-8, National Institute for Materials Science, Sayo, Hyogo 679-5148, Japan*

Jaemyung Kim − *Synchrotron X-ray Group and Synchrotron X-ray Station at SPring-8, National Institute for Materials Science, Sayo, Hyogo 679-5148, Japan;* orcid.org/0000-0002-3298-2972

Satoshi Hiroi − *Synchrotron X-ray Group and Synchrotron X-ray Station at SPring-8, National Institute for Materials Science, Sayo, Hyogo 679-5148, Japan*

Osami Sakata − *Synchrotron X-ray Group and Synchrotron X-ray Station at SPring-8, National Institute for Materials Science, Sayo, Hyogo 679-5148, Japan;* orcid.org/0000-0003-2626-0161

Tomokazu Yamamoto − *Department of Applied Quantum Physics and Nuclear Engineering, Kyushu University, Fukuoka 819-0395, Japan; The Ultramicroscopy Research Center, Kyushu University, Fukuoka 819-0395, Japan*

Syo Matsumura − *Department of Applied Quantum Physics and Nuclear Engineering, Kyushu University, Fukuoka 819-0395, Japan; The Ultramicroscopy Research Center, Kyushu University, Fukuoka 819-0395, Japan*

Yusuke Nanba − *Center for Green Research on Energy and Environmental Materials, National Institute for Materials Science, Ibaraki 305-0044, Japan; Research Initiative for Supra-Materials, Shinshu University, Nagano, Nagano 380-8553, Japan;* orcid.org/0000-0002-1692-4465

Michihisa Koyama − *Center for Green Research on Energy and Environmental Materials, National Institute for Materials Science, Ibaraki 305-0044, Japan; Research Initiative for Supra-Materials, Shinshu University, Nagano, Nagano 380-8553, Japan*

Naoki Ogiwara − *Division of Chemistry, Graduate School of Science, Kyoto University, Kyoto 606-8502, Japan;* Present Address: Department of Basic Science, School of Arts and Sciences, The University of Tokyo, 3-8-1 Komaba, Meguro-ku, Tokyo 153-8902, Japan

Shogo Kawaguchi − *Research & Utilization Division, Japan Synchrotron Radiation Research Institute (JASRI), Sayo-gun, Hyogo 679-5198, Japan*

Yoshiki Kubota − *Department of Physical Science, Graduate School of Science, Osaka Prefecture University, Sakai, Osaka 599-8531, Japan*

Complete contact information is available at: https://pubs.acs.org/10.1021/acsmaterialsau.1c00048

Author Contributions

The manuscript was written through contributions of all authors.

Notes

D.W., K.K., and H.K. have a patent application, "PdRu solid solution nanoparticles, method for producing the same and catalyst, method for controlling crystal structure of PtRu solid solution nanoparticles, and AuRu solid solution nanoparticles and method for producing the same" (JPWO2018159644A1). The authors declare no competing financial interest.

■ ACKNOWLEDGMENTS

We acknowledge the support from JST ACCEL program Grant Number JPMJAC1501 and Grant-in-Aid for Specially Promoted Research 20H05623. STEM observations were performed as a part of a program conducted by the Advanced Characterization Nanotechnology Platform sponsored by the MEXT of the Japanese Government. Synchrotron XRD measurements were carried out at SPring-8 beamline BL02b2 under Proposal No. 2014B1382, 2015A1586, and 2016A1483. The Pd and Ru K-edge XAFS experiments were performed at SPring-8 beamline BL14b2.

■ ABBREVIATIONS

NPs, nanoparticles; fcc, face-centered cubic; hcp, hexagonal close-packed; LSV, linear sweep voltammetry; VB, valence band; HAXPES, hard X-ray photoelectron spectroscopy; FE, Faraday efficiency; OER, oxygen evolution reaction; XANES, X-ray absorption near-edge spectra; ADT, accelerated durability test

■ REFERENCES

(1) Cox, P. A. *The electronic structure and chemistry of solids*; Oxford University Press: Oxford, 1987.
(2) Cheng, H.; Yang, N.; Lu, Q.; Zhang, Z.; Zhang, H. Syntheses and properties of metal nanomaterials with novel crystal phases. *Adv. Mater.* **2018**, *30*, 1707189.
(3) Zhao, M.; Xia, Y. Crystal-phase and surface-structure engineering of ruthenium nanocrystals. *Nat. Rev. Mater.* **2020**, *5*, 440−459.
(4) Wu, D.; Kusada, K.; Kitagawa, H. Recent progress in the structure control of Pd−Ru bimetallic nanomaterials. *Sci. Technol. Adv. Mater.* **2016**, *17*, 583−596.
(5) Tripathi, S.; Bharadwaj, S.; Dharwadkar, S. The Pd-Ru system (palladium-ruthenium). *J. Phase Equilib.* **1993**, *14*, 638−642.
(6) Wu, D.; Cao, M.; Shen, M.; Cao, R. Sub-5 nm Pd−Ru nanoparticle alloys as efficient catalysts for formic acid electro-oxidation. *ChemCatChem* **2014**, *6*, 1731−1736.
(7) Kusada, K.; et al. Solid solution alloy nanoparticles of immiscible Pd and Ru elements neighboring on Rh: changeover of the thermodynamic behavior for hydrogen storage and enhanced CO-oxidizing ability. *J. Am. Chem. Soc.* **2014**, *136*, 1864−1871.
(8) Zhang, Q.; et al. Selective control of fcc and hcp crystal structures in Au-Ru solid-solution alloy nanoparticles. *Nat. Commun.* **2018**, *9*, 510.
(9) *NIST X-ray Photoelectron Spectroscopy Database*; National Institute of Standards and Technology, Gaithersburg, MD. DOI: 10.18434/T4T88K.
(10) Pettifor, D. A Physicist's view of the energetics of transition metals. *CALPHAD: Comput. Coupling Phase Diagrams Thermochem.* **1977**, *1*, 305−324.
(11) Reier, T.; Oezaslan, M.; Strasser, P. Electrocatalytic Oxygen Evolution Reaction (OER) on Ru, Ir, and Pt Catalysts: A Comparative Study of Nanoparticles and Bulk Materials. *ACS Catal.* **2012**, *2*, 1765−1772.
(12) Nong, H. N.; et al. Oxide-supported IrNiO(x) core-shell particles as efficient, cost-effective, and stable catalysts for electrochemical water splitting. *Angew. Chem., Int. Ed.* **2015**, *54*, 2975−2979.
(13) Kim, J.; et al. High-Performance Pyrochlore-Type Yttrium Ruthenate Electrocatalyst for Oxygen Evolution Reaction in Acidic Media. *J. Am. Chem. Soc.* **2017**, *139*, 12076−12083.
(14) Seitz, L. C.; et al. A highly active and stable IrOx/SrIrO3 catalyst for the oxygen evolution reaction. *Science* **2016**, *353*, 1011−1014.
(15) Pi, Y.; et al. Ultrathin laminar Ir superstructure as highly efficient oxygen evolution electrocatalyst in broad pH range. *Nano Lett.* **2016**, *16*, 4424−4430.
(16) Oh, H.; et al. Electrochemical Catalyst−Support Effects and Their Stabilizing Role for IrOx Nanoparticle Catalysts during the Oxygen Evolution Reaction. *J. Am. Chem. Soc.* **2016**, *138*, 12552−12563.
(17) Su, J.; et al. Assembling Ultrasmall Copper-Doped Ruthenium Oxide Nanocrystals into Hollow Porous Polyhedra: Highly Robust Electrocatalysts for Oxygen Evolution in Acidic Media. *Adv. Mater.* **2018**, *30*, 1801351−1801358.
(18) Fu, L.; et al. Ultrathin Ir nanowires as high-performance electrocatalysts for efficient water splitting in acidic media. *Nanoscale* **2018**, *10*, 1892−1897.
(19) Li, T.; et al. Atomic-scale insights into surface species of electrocatalysts in three dimensions. *Nat. Catal.* **2018**, *1*, 300.
(20) Danilovic, N.; et al. Activity-Stability Trends for the Oxygen Evolution Reaction on Monometallic Oxides in Acidic Environments. *J. Phys. Chem. Lett.* **2014**, *5*, 2474−2478.
(21) Over, H. Surface chemistry of ruthenium dioxide in heterogeneous catalysis and electrocatalysis: from fundamental to applied research. *Chem. Rev.* **2012**, *112*, 3356−3426.
(22) Wu, D.; et al. Efficient overall water splitting in acid with anisotropic metal nanosheets. *Nat. Commun.* **2021**, *12*, 1145.
(23) Chang, S. H.; et al. Functional links between stability and reactivity of strontium ruthenate single crystals during oxygen evolution. *Nat. Commun.* **2014**, *5*, 4191.
(24) Reuter, K.; Ganduglia-Pirovano, M.; Stampfl, C.; Scheffler, M. Metastable precursors during the oxidation of the Ru(0001) surfaces. *Phys. Rev. B: Condens. Matter Mater. Phys.* **2002**, *65*, 165403.
(25) Reuter, K.; Stampfl, C.; Ganduglia-Pirovano, M.; Scheffler, M. Atomistic description of oxide formation on metal surfaces: the example of ruthenium. *Chem. Phys. Lett.* **2002**, *352*, 311−317.
(26) Rossmeisl, J.; Logadottir, A.; Nørskov, J. K. Electrolysis of water on (oxidized) metal surfaces. *Chem. Phys.* **2005**, *319*, 178−184.
(27) Liu, J.; Su, H.; Sun, D.; Zhang, B.; Li, W. Crystallographic dependence of CO activation on cobalt catalysts: HCP versus FCC. *J. Am. Chem. Soc.* **2013**, *135*, 16284−16287.
(28) Kawaguchi, S.; et al. High-throughput powder diffraction measurement system consisting of multiple MYTHEN detectors at beamline BL02B2 of SPring-8. *Rev. Sci. Instrum.* **2017**, *88*, 085111.
(29) Lee, Y.; Suntivich, J.; May, K. J.; Perry, E. E.; Shao-Horn, Y. Synthesis and activities of rutile IrO_2 and RuO_2 nanoparticles for oxygen evolution in acid and alkaline solutions. *J. Phys. Chem. Lett.* **2012**, *3*, 399−404.